Post-print of: Głowienka D., Szmytkowski J.: Numerical modeling of exciton impact in two crystalographic phases of the organo-lead halide perovskite (CH3NH3PbI3) solar cell. SEMICONDUCTOR SCIENCE AND TECHNOLOGY. Vol. 34, iss. 3 (2019), 035018 (14pp). DOI: 10.1088/1361-6641/aafeef

Numerical modeling of exciton impact in two crystalographic phases of the organo–lead halide perovskite ($CH_3NH_3PbI_3$) solar cell[†]

Damian Głowienka & Jędrzej Szmytkowski

Faculty of Applied Physics and Mathematics, Gdańsk University of Technology, Narutowicza 11/12, 80-233 Gdańsk,

E-mail: dglowienka@mif.pg.gda.pl

December 2018

Abstract. To improve the power conversion efficiency of solar cells based on organo–lead halide perovskites, a detailed understanding of the device physics is fundamental. Here, a computational analysis of excitons impact is reported for this type of photocells. Numerical calculations based on the model which takes into account electronic charge carriers (electrons and holes), excitons and ions have been carried out. The role of excitons in two crystallographic phases associated with different temperatures (80 K and 295 K) has been studied with the Saha relation, which clearly distinguishes a domination of free charge carriers or excitons. We have confirmed that excitons prevail in orthorombic phase. Our work provides information about photophysics of the lead halide perovskite, which allows to better understand the operation of devices based on the perovskite material.

1. Introduction

The methylammonium lead iodide perovskite crystals ($CH_3NH_3PbI_3$) have recently gain an attention due to their extraordinary power conversion efficiency, which has already approached values over 23%[1–3]. Such a tremendous efficiency of the organometal trihalide perovskite (OTP) solar cells derives from their optical and electrical properties, like the large light absorption coefficient, high mobilities and long diffusion lengths of charge carriers[4–7]. However, to achieve the highest efficiency of energy conversion, it is required to recognize all physical mechanisms which play a key role in the device operation.

It seems that organo–lead halide perovskite materials are likely non–excitonic in the room temperature. This conclusion is based on a very low effective mass and a high dielectric constant which lead to lower binding energy of Wannier exciton ($\approx$ 6 meV) in comparison to thermal energy ($\approx$ 26 meV)[8–12]. Therefore, a stability of this exciton would be extremely small. However, the electrical and transport properties of trihalide perovskites may drastically change with phase transition[13]. Three phases of

the OTP material are observed in different temperature regimes[14–16]. The orthorhombic phase is present at a low temperature and converts into tetragonal phase at about 160 K. The transition between tetragonal and cubic phases takes place above 330 K[17–19]. The binding energy of exciton increases to about 16–50 meV in orthorhombic phase. Therefore, Wang et al.[20] have recently suggested that perovskite semiconductor may be excitonic in low temperatures due to higher exciton binding energy than the thermal energy ($\approx$ 6 meV at 80 K)[10,21]. This may have direct implication in low temperature applications like in space environment for powering sattelites[22]. However, an exact role of excitons in the organo–lead halide perovskites requires better recognition and detailed understanding.

Here, we make numerical studies to examine processes concerning excitons with a special focus on their formation mechanism. The results of simulations are compared to the OTP solar cell ($CH_3NH_3PbI_3$). In the paper, we apply one dimensional transient model based on drift–diffusion equations for electronic charge carriers (electrons and holes), ions and excitons. Although the drift–diffusion model has been widely used to simulate organic photovoltaic cells[23–26] and recently also for the organo–lead halide perovskite solar cells[27–33], we are the first (as to our knowledge) who included both ions and excitons for the perovskite materials. We decided to analyze a perovskite photocell in tetragonal (295 K) and orthorhombic (80 K) phases. The choice of temperature is based on accessibility of literature data for the OTP material.

2. Model

For the purpose of the model, it is assumed that electron and hole transporting layers, which are usually used in perovskite solar cells, generate no losses of charge carriers. This allows us to simulate processes which occur only in the perovskite layer.

In the model, excitons are assumed to be immobile due to a very short lifetime. In addition, there is no information in literature about experimental observation of mobile excitons in the perovskite materials. Thus, to describe time (t) dependent excitonic processes, the continuity equation looks as follows[34,35]

$$\frac{\partial S}{\partial t} = k_f np - k_d S - \frac{S}{\tau_S}, \tag{1}$$

where S is a concentration of excitons which can be formed from electrons and holes with bimolecular formation rate k_f. The excitons also dissociate with a rate k_d and recombine monomolecularly (radiatively and nonradiatively) with a decay time τ_S.
The system of equations for transport of electronic charges is based on continuity equations for electrons and holes, which are given by

$$\frac{\partial n}{\partial t} = G + k_d S - k_f np - R_m - R_b - R_t + \frac{1}{q}\frac{\partial}{\partial x} J_n, \tag{2}$$

$$J_n = -qn\mu_n \frac{\partial \phi}{\partial x} + \mu_n k_B T \frac{\partial n}{\partial x}, \tag{3}$$

$$\frac{\partial p}{\partial t} = G + k_d S - k_f np - R_m - R_b - R_t - \frac{1}{q}\frac{\partial}{\partial x} J_p, \tag{4}$$

$$J_p = -qp\mu_p \frac{\partial \phi}{\partial x} - \mu_p k_B T \frac{\partial p}{\partial x}, \tag{5}$$

where n and p are electron and hole concentrations, respectively, q represents elementary charge, k_B is a Boltzmann constant, J_n and J_p are electron and hole currents, respectively, T represents absolute temperature of simulated sample, ϕ is an electric potential, μ_n and μ_p are mobilities of electrons and holes, respectively, and x represents space position. The parameter G denotes generation rate of free carriers, whereas R_m, R_b and R_t are monomolecular, bimolecular and trimolecular recombination rates, respectively.

The equations which describe behavior of ions can be written as[33]

$$\frac{\partial a}{\partial t} = \frac{1}{q}\frac{\partial}{\partial x}\left(-qa\mu_a \frac{\partial \phi}{\partial x} + \mu_a k_B T \frac{\partial a}{\partial x}\right) \tag{6}$$

and

$$\frac{\partial c}{\partial t} = -\frac{1}{q}\frac{\partial}{\partial x}\left(-qc\mu_c \frac{\partial \phi}{\partial x} - \mu_c k_B T \frac{\partial c}{\partial x}\right), \tag{7}$$

where a and c are densities of anions and cations, respectively, whereas μ_a and μ_c represent mobilities of these ions. The currents of anions (J_a) and cations (J_c) are symmetrical as in the case of electrons and holes.

The simulated charge carriers densities are linked with the Poisson equation for potential distribution

$$\frac{\partial^2 \phi}{\partial x^2} = -\frac{q}{\varepsilon_0 \varepsilon_r}\left(p - n + c - a\right), \tag{8}$$

where ε_0 is a vacuum permittivity and ε_r represents dielectric constant of the analyzed material. The electric field (E) can be calculated from the relation $E = -\partial\phi/\partial x$.

The total current is recorded at each time step

$$\begin{aligned} J(x,t) =& qE\left(n\mu_n + p\mu_p + a\mu_a + c\mu_c\right) + \\ &+ k_B T\left(\mu_n \frac{\partial n}{\partial x} - \mu_p \frac{\partial p}{\partial x} + \mu_a \frac{\partial a}{\partial x} - \mu_c \frac{\partial c}{\partial x}\right) + \\ &+ \varepsilon_0 \varepsilon_r \frac{\partial E}{\partial t} \end{aligned} \tag{9}$$

in every position x. To obtain the J–V characteristics for simulated solar cell, the current density is averaged throughout the device.

The rate of exciton dissociation into separated charge carriers is based on the thermal model[11,35]

$$k_d = \frac{E_B}{h}\exp\left(-\frac{E_B}{k_B T}\right), \tag{10}$$

where h represents Planck's constant and E_B is the binding energy of exciton.
The recombination of charge carriers can be described as monomolecular, bimolecular and trimolecular processes. The monomolecular recombination rate is defined by the Shockley–Read–Hall (SRH) model[36]

$$R_m = \frac{C_n C_p N_t}{C_n\left(n+n_1\right)+C_p\left(p+p_1\right)}\left(np-n_{int}^2\right), \tag{11}$$

where C_n and C_p are charge trapping rates for electrons and holes, respectively. The parameter N_t represents a trap density of the energy level $E_t = E_g/2$ placed in between band–gap defined as $E_g = E_c - E_\nu$. The energies E_c and E_ν denote edges of conduction and valence bands, respectively. We assume that the traps are located in the mid–gap where they are the most efficient recombination centers[37]. The characteristic carrier densities of electrons $n_1 = N_c \exp\left[\left(E_t - E_c\right)/k_B T\right]$ and holes $p_1 = N_\nu \exp\left[\left(E_\nu - E_t\right)/k_B T\right]$ are defined for the case when the Fermi level coincides with the energy of recombination center E_t. The intrinsic charge carrier concentration can be written as $n_{int} = \left(N_c N_\nu\right)^{1/2} \exp\left(-E_g/2k_B T\right)$, where N_c and N_ν are effective densities of states in conduction and valence bands, respectively.
The bimolecular recombination rate is based on the modified Langevin model[38]

$$R_b = \xi \frac{q}{\varepsilon_0 \varepsilon_r}\left(\mu_n + \mu_p\right)\left(np - n_{int}^2\right), \tag{12}$$

where ξ is a recombination reduction factor ($\xi \leq 1$).
The trimolecular recombination rate of charge carriers can be treated as an Auger process[39], described by electron Γ_n and hole Γ_p recombination constants

$$R_t = \left(\Gamma_n n + \Gamma_p p\right)\left(np - n_{int}^2\right). \tag{13}$$

For spatial boundary conditions of electronic charge carriers and electrical potential, there are distinguished two specific positions. At the anode ($x = 0$), the boundary conditions are expressed by

$$n(0) = N_c \exp\left(-\frac{\phi_n}{k_B T}\right), \tag{14}$$

$$p(0) = N_\nu \exp\left(\frac{\phi_n - E_g}{k_B T}\right), \tag{15}$$

$$\phi(0) = V_{build} - V_a, \tag{16}$$

where ϕ_n is an injection barrier at the anode, V_{built} represents built–in voltage and V_a is an externally applied voltage. At the cathode ($x = L$), we can write

$$n(L) = N_c \exp\left(\frac{\phi_p - E_g}{k_B T}\right), \tag{17}$$

$$p(L) = N_\nu \exp\left(-\frac{\phi_p}{k_B T}\right), \tag{18}$$

$$\phi(L) = 0. \tag{19}$$

where ϕ_p is an injection barrier at the cathode. In the model, there is no current injection at $J_n(x = L)$ for electrons and at $J_p(x = 0)$ for holes. We have also assumed that the ion currents J_a and J_c are zero at both electrodes.
The time boundary conditions ($t = 0$) for concentrations of electrons and holes are assumed to be zero. However, for the case of ion densities, we should note that ions cannot migrate outside the active layer of perovskite material. Thus, initial densities of anions and cations are

$$a\,(t = 0) = N_0, \quad c\,(t = 0) = N_0. \tag{20}$$

In addition, the change of ions concentrations at both electrodes can be defined as

$$\left.\frac{\partial a}{\partial x}\right|_{x=0,L} = 0, \quad \left.\frac{\partial c}{\partial x}\right|_{x=0,L} = 0. \tag{21}$$

It should be mentioned that the existence of electrons, holes and ions in one material causes nomenclature discrepancies in the names of electrodes. According to a standard definition, positively charged ions (cations) move toward the cathode and negatively ions (anions) flow in opposite direction. Thus, the positions of cathode and anode have been found as a result of temporal simulations where we investigated the accumulation of anions (mobile ions in the perovskite) near electrodes.

The drift–diffusion model is discretized with Scharfetter–Gummel[40] method and solved with C++ language [see equations (S1–S7) in Supplementary data]. The continuity equations are solved by forward iteration in time, and the resulted drift–diffusion and displacements currents are found for each iteration. The process is continued until steady–state condition is reached [see equation (S9) in Supplementary data]. We should note that the existence of ionic charge carriers in the sample introduces a problem with a very long computing time. The reason is that ions are extremely slow in comparison to electronic charge carriers in perovskite solar cells[30]. The influence of ions on excitons is not studied here, therefore mobilities of ions can be set for higher values to increase the computation speed[28]. However, a special care must be taken for such dynamic simulations. In the transient calculations, the generation rate is first set to zero ($G = 0$) and the simulations last until steady state is achieved. At this moment charge carriers and ions are at thermodynamical equilibrium. In addition, ions should already finish to migrate through the sample just before illumination and futher simulations are not influencing their behaviour to a greater extent. Afterwards, the sunlight (AM1.5G) is turned on ($G \neq 0$) and each iteration is recorded[26]. In all simulations, the timestep is

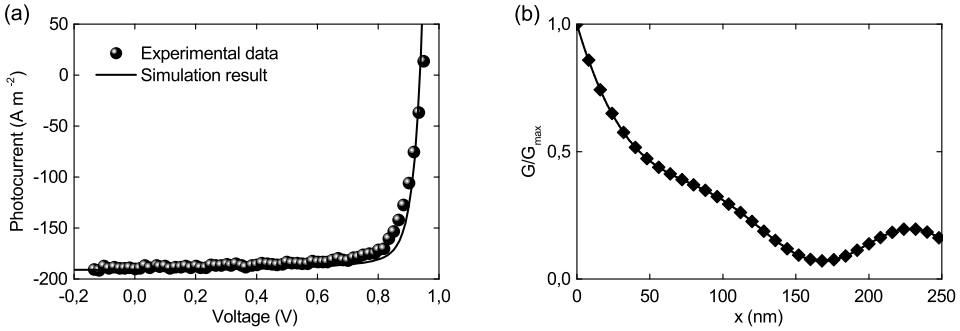

Figure 1. a) J–V characteristics for the absorber thickness 250 nm. The solid line represents the simulation and sphere points show the experimental data for $CH_3NH_3PbI_3$ at 295 K, obtained from Ref. 42. b) Generation (G) profile used in the simulation and calculated using the transfer matrix model. It is normalized with G_{max}.

set to 1 ps due to relatively high dynamics of exciton processes. The spatial grid is non–uniformly distributed with Chebyshev polynomial [see equation (S11) in Supplementary data]. It makes possible to dense the grid closely to contacts where the most abrupt changes are observed. All parameters have been fixed in space which seems to be a good approximation that has been already used for simulation of perovskite[27,29] and other materials[24,41].

3. Results and discussion

The model validation has been performed with a fit to experimental data for p-i-n structure with little or no hysteresis[42]. The configuration of investigated device looks as follows: ITO/HTL/$CH_3NH_3PbI_3$/ETL/Al, where PEDOT:PSS is used for the hole transporting layer (HTL), and PCBM, C_{60} and BCP for the electron transporting layer (ETL). As mentioned earlier, the device stack has been modeled with only perovskite layer. Thus, we can assume that ETL and HTL are at the same electric potential levels as the interface of perovskite[30]. The model is sensitive for fitting, therefore a perovskite layer with three thicknesses 250, 280 and 630 nm were simulated with a single set of device parameters to find reasonable values. These values are used as a starting point for the following numerical simulations. Figure 1(a) shows a comparison between theoretical and experimental results for a thickness 250 nm. A good agreement has been obtained. The fitting results for 280 and 630 nm are presented in figure S1 (Supplementary data) with corresponding generation profiles. We can see that the fit is in excellent agreement with experimental results obtained for a thickness 280 nm. However, the J–V slope is slightly shifted for the case of 630 nm. This may be due to neglecting of interface effects. However, we focus only on the excitonic phenomena in the bulk, therefore the contact effects may be ignored.

The data used in the fitting procedure are written in table 1 with corresponding references to parameters for $CH_3NH_3PbI_3$. The mobilities are asymmetrical and within

Table 1. Parameters used in the fitting of the experimental data and simulations at 295 K.

Parameter	Symbol	Value	
Dielectric constant	ε_r	63.05	Ref. 15
Thickness of active material	L	250 nm	Ref. 42
Exciton binding energy	E_B	6 meV	Ref. 8
Exciton formation rate	k_f	10^{-12} m^3 s^{-1}	Ref. 35
Exciton decay time	τ_s	44 ps	Ref. 20
e^- and h^+ capture coefficients	C_n, C_p	1.5×10^{-14} m^3 s^{-1}	Ref. 14
Reduction factor	ξ	10^{-4}	Ref. 29
e^- and h^+ Auger constants	Γ_n, Γ_p	1.55×10^{-40} m^6 s^{-1}	Ref. 14
Edge of conduction band	E_c	-3.9 eV	Ref. 43
Edge of valence band	E_ν	-5.4 eV	Ref. 43
Injection barrier heights	ϕ_n, ϕ_p	0.1 eV	Ref. 31
Initial density of ions	N_0	10^{23} m^{-3}	Ref. 30
Trap density	N_t	10^{21} m^{-3}	Ref. 14
e^- and h^+ density of states	N_c, N_ν	8.1×10^{24} m^{-3}	Ref. 31
Mobility of anions	μ_a	10 cm^2 V^{-1} s^{-1}	Ref. 28
Mobility of electrons	μ_n	4 cm^2 V^{-1} s^{-1}	Fit
Mobility of holes	μ_p	3 cm^2 V^{-1} s^{-1}	Fit
Built-in voltage	V_{built}	1.23 V	Fit
Maximum generation rate	G_{max}	1.55×10^{28} m^{-3} s^{-1}	Fit
Timestep	Δt	1 ps	Fixed
Number of grid points		100	Fixed

reported values[4,16]. To fit a short–circuit photocurrent, the maximum charge generation rate is slightly changed and, for an open–voltage, the built–in voltage is fitted.

The transfer matrix model[44,45] has been applied to calculate the generation profile G presented in figure 1(b). In this optical model, the thickness of each layer used in the solar cell is given with a correlated extinction coefficient (κ) and a refractive index (η); see references in table S1 (Supplementary data). The fitting could be also performed with a constant value of G (uniform generation profile), however the loss of absorbed light within the thick sample of OTP solar cell is high. Therefore, a nonuniform generation should be used (see figure S2 in Supplementary data).

The ions are located only within a perovskite layer in the p-i-n structure. Obviously, anions and cations can change an electric field distribution in the bulk of sample. It should be noted that the experimental data could be also well fitted with immobile ions (as shown in figure S5 in Supplementary data) using parameters adopted from literature (table 1).

The next two paragraphs for 295 K and 80 K are organized in the following manner. First, we analyze spatial impact of excitons on perovskite solar cell at steady–state condition with continuous AM1.5 light illumination. Further, the dynamic simulations are shown. Also, if not specified otherwise, the parameters from table 1 are used in all simulations.

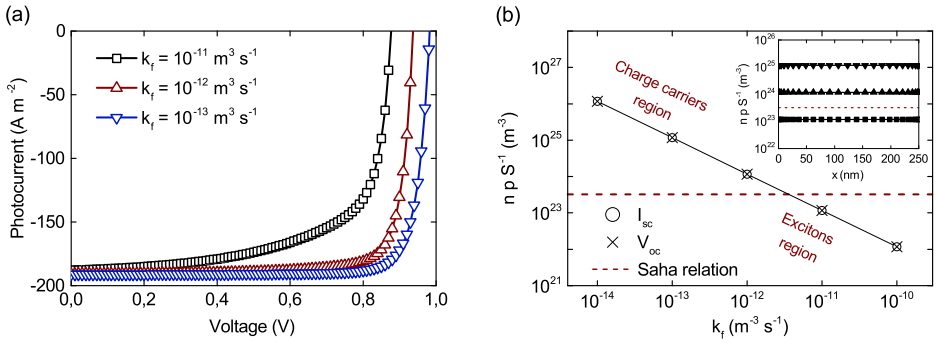

Figure 2. Simulation results for different exciton formation parameters at 295 K. a) J–V characteristics, b) a Saha relation for J_{sc} (circle symbol) and V_{oc} (cross symbol) with red line showing equilibrium level between charge carriers and excitons. An inset shows spatial distribution of Saha relation. Squares, upper triangles and lower triangles denote the exciton formation rates (k_f) equal to 10^{-11}, 10^{-12} and 10^{-13} m^3 s^{-1}, respectively.

3.1. Results for 295 K

To analyze the exciton impact in perovskite solar cells, we decided to choose three values of the exciton formation rate: 10^{-11}, 10^{-12} and 10^{-13} m^3 s^{-1}, called in the paper high, intermediate and low formation rates, respectively. The values are chosen based on $k_f = 10^{-12}$ m^3 s^{-1} that is close to the experimental result estimated by Stranks et al[35]. Figure 2(a) shows the J–V characteristics calculated for these three values of k_f. It is observed that the magnitude of J_{sc} is changed negligibly with k_f but a value of V_{oc} calculated for the high and low rates changes by about 0.05 V in respect to the intermediate formation rate. This may have practical implication for further analysis of losses for an open–circuit (OC) condition.

As the impact of excitons is not clearly visible in the spatial distribution in the bulk of perovskite material, the appropriate tool is needed. Therefore, the Saha equation[11,12,46,47] is applied to distinguish whether excitons or free charge carriers dominate in the OTP solar cell. It has the form

$$\frac{np}{S} = n_{eq}(T) = \left(\frac{2\pi\mu_S k_B T}{h^2}\right)^{3/2} \exp\left(-\frac{E_B}{k_B T}\right), \tag{22}$$

where n_{eq} represents the equilibrium state which means that the densities of electrons, holes and excitons are equal ($n = p = S$). The reduced effective mass can be defined as $\mu_S = m_e m_h / (m_e + m_h)$, where m_e and m_h are effective masses of electron and hole, respectively. An interpretation of the Saha equation is that excitons prevail below n_{eq} and the free charge carriers are dominant above this value. Figure 2(b) presents a graphical illustration of the Saha equation where the ratio np/S is calculated for different exciton formation rates. The dashed line shows the equilibrium state n_{eq} calculated for the exciton binding energy equal to 6 meV for 295 K (see Ref. 8) and the reduced effective mass 0.104 m$_e$ reported for the $CH_3NH_3PbI_3$ perovskite[10]. For all cases, we

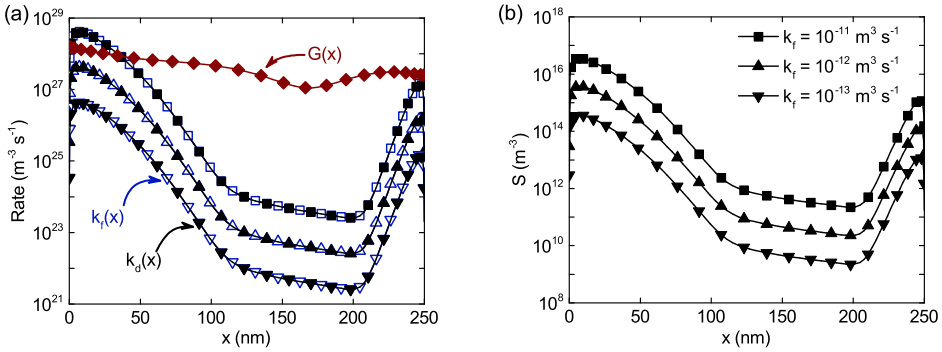

Figure 3. Simulation results for short–circuit current (J_{sc}) at 295 K. a) Exciton formation, dissociation and charge carrier generation rates, b) exciton density distribution. The diamond symbols indicate a rate of charge carriers generation. Squares, upper triangles and lower triangles denote the exciton formation rates (k_f) equal to 10^{-11}, 10^{-12} and 10^{-13} m^3 s^{-1}, respectively. The closed symbol is used for formation rate and open symbol represents dissociation rate of excitons.

obtained constant values of np/S presented by horizontal lines [see figure 2(b-inset)]. It is clearly seen that charge carriers prevail for the low and intermediate exciton formation rate and excitons are in dominance only for the high value of k_f. We should also mention that the Saha relation looks the same for J_{sc} and V_{oc} because it does not depend on the bias voltage, as shown in figure 2.

Generally, under the short–circuit (SC) condition, all losses are lower than a generation of electrons and holes for integration over the entire device. This condition is self consistent for the model. Whereas for OC, both recombination and generation should be equal[29]. Therefore, the case when the sum of all recombination rates is greater than the generation rate has no physical sense. Figure 3(a) presents a comparison of a charge generation rate (G) with the rates $k_f \times np$ and $k_d \times S$, which are associated with the exciton formation and the exciton dissociation, respectively, all calculated for J_{sc}. It is seen that for a high value of k_f, the formation rate ($k_f \times np$) averaged in space (6.64×10^{27} m^{-3} s^{-1}) is slightly higher than the generation rate (5.85×10^{27} m^{-3} s^{-1}). Based on this observation, it can be concluded that although the Saha equation shows a domination of excitons [figure 2(b)], the case with $k_f = 10^{-11}$ m^3 s^{-1} is not physical. This also shows the maximum limit for the formation rate of excitons at room temperature. We also observe that the formation and dissociation rates follow the same dynamics for the equilibrium state which was recently suggested by Stranks et al.[35]. Therefore, excitons are created and lost within the same period of time due to their low binding energy. As shown in figure 3, the shape of the formation rate follows the shape of the excitons distribution in space. This behavior can be explained this way that excitons are generated only as a result of the formation process; see equation (1).

We can see that nonuniform generation rate leads to irregular shape of the excitons distribution in space for SC condition. In addition, an electric potential and, as a consequence, an electric field depend on the distributions of all types of electric charges

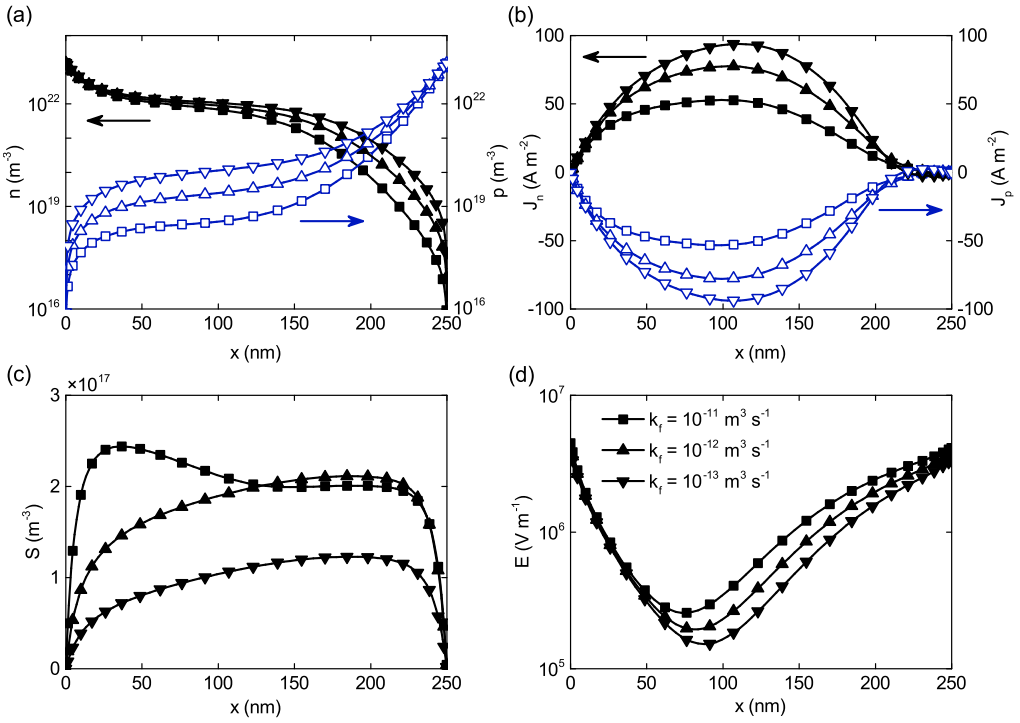

Figure 4. Simulation results for open–circuit (V_{oc}) at 295 K. Spatial distributions for a) electrons (closed symbol) and holes (open symbol) concentrations, b) electron (closed symbol) and hole (open symbol) photocurrents, c) exciton concentration, and d) electric field. Squares, upper triangles and lower triangles denote the exciton formation rates (k_f) equal to 10^{-11}, 10^{-12} and 10^{-13} m^3 s^{-1}, respectively.

(electrons, holes and both types of ions) which, in general, are mobile with different mobilities. Thus, we can expect further irregularities in simulated curves which can create problems with an exact analysis. Therefore, we have decided to simulate also curves with uniform generation rate and with immobile ions. These results obtained for 295 K are presented in Supplementary data (figures S2–S9). Figure S2 illustrates the J–V characteristics and the Saha relation calculated for uniform and nonuniform generation. The comparison shows negligible differences in shapes. However, the nonuniform generation has a great impact on the distributions of photocurrents J_n and J_p which follow the shape of the generation profile [shown for short–circuit in figure S3(b)]. It can be also noticed that the value of photocurrent at a maximum point (for OC condition) is much higher than for organic solar cell; see figure S4(b)[23,48]. This is directly caused by a nonuniform generation and a thicker absorber layer. The immobile ions slightly change the J–V characteristics and do not impact the Saha relation (see figure S5). Additionally, there are only small changes observed for J_n and J_p distributions for mobile and immobile ions, as shown in figure S6. However, for SC condition, the mobile ions influence charge carrier concentrations by increasing density of electrons in the middle of OTP cell; see figure S7(c). We can also see that a concentration of mobile anions (a) decreases drastically in the bulk of sample [figure S7(a)]. Therefore,

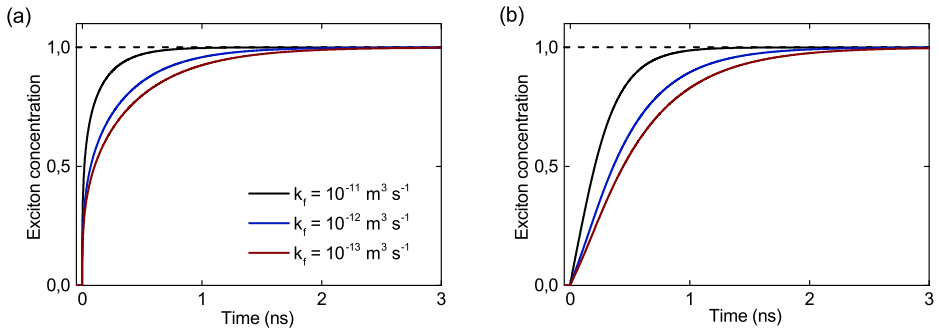

Figure 5. Simulation results for open–circuit (V_{oc}) at 295 K. Transient results for exciton concentration a) at the position close to the anode, and b) in the middle of sample. Black, blue and red lines denote the exciton formation rates (k_f) equal to 10^{-11}, 10^{-12} and 10^{-13} m^3 s^{-1}, respectively. All results are normalized.

the electric field distribution changes visibly in comparison to the case of immobile ions, as illustrated in figure S7(b). For an open–circuit, a similar change of the electric field is also observed, where a minimum of $E(x)$ is still shifted toward the anode [see figure S8(b)]. We can see that the exciton concentration in space is symmetrical when ions are immobile and becomes asymmetrical for a case of mobile anions. The position of the maximum in the distribution of excitons coincides with the observed changes of electrons and holes concentrations close to the cathode; see figures S8(c–d). However, for a high value of k_f, we observe a different shape of the exciton distribution in space with a maximum which appears near the anode, as seen in figure S9.

Figure 4 presents simulation results calculated for three values of the exciton formation rate in the case of OC. As it is observed in figure 4(a), an increase of the formation parameter lowers the density of electrons and holes which directly impacts the V_{oc} level in the same way. This behavior could be explained by the mechanism of exciton formation, where an electron and a hole interact with each other and create an exciton with a probability related to the formation rate [see equation (1)]. It has been proved that excitons dissociate with the same rate for SC [figure 3(a)]. Therefore only negligible changes in electrons and holes distributions, and their photocurrents are observed (see figure S10 in Supplementary data). However, under OC condition, where an electric field is much lower inside the OTP solar cell, the exciton formation and the dissociation rates are not equal (results not shown here). Thus, excitons can also recombine monomolecularly within their lifetime τ_S. Consequently, not all free electrons and holes are produced back from excitons which results in lowering their densities. Due to changes of these concentrations, the space distributions of photocurrents are also influenced. For the higher exciton formation rate, the electron (J_n) and the hole (J_p) photocurrents decrease about the zero axis [see figure 4(b)]. These distributions are likely lowered due to observed changes of electric field with increasing rate of exciton formation [figure 4(d)]. As shown in figure 4(c), the exciton density increases uniformly across the material, if changed from low to intermediate values of

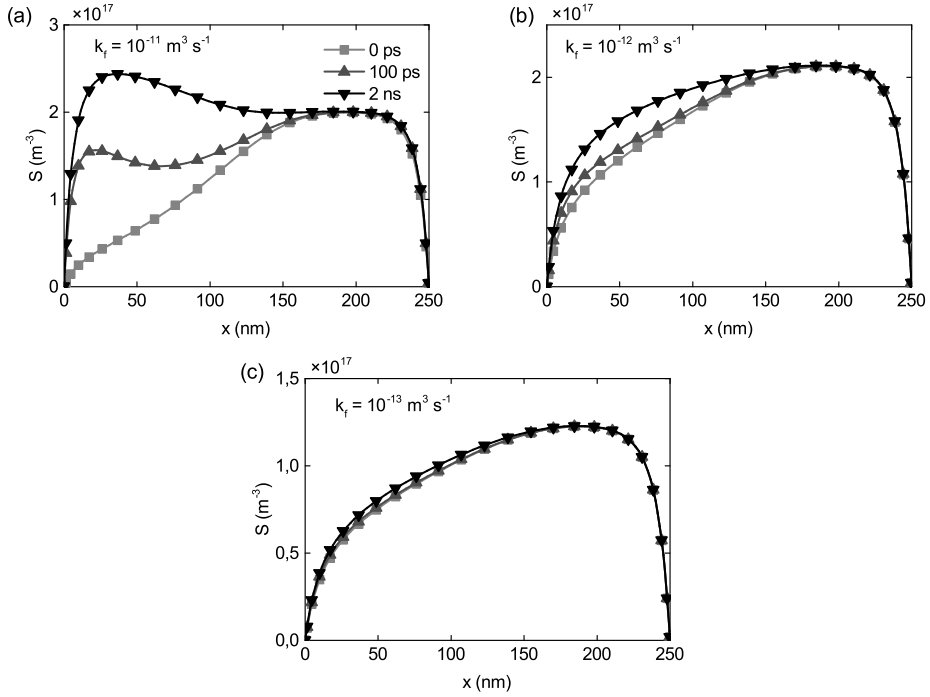

Figure 6. Simulation results for open–circuit (V_{oc}) at 295 K. Spatial distribution for formation rates (k_f) equal to a) 10^{-11}, b) 10^{-12}, and c) 10^{-13} m^3 s^{-1}. Squares, upper triangles and lower triangles denote spatial distributions for 0 ps, 100 ps and 2 ns, respectively, which is a time since generation was turned on ($G \neq 0$).

formation rate. However, the shape of this distribution changes drastically for a high k_f. The explanation for this behavior will be provided in further part of the paper with a discussion of dynamical simulation results.

The next step is to analyze transient results to get more insight into process of exciton formation. Figure 5 shows results of the normalized exciton concentrations close to an electrode position (part a) and in the middle of the sample (part b), both presented for an open–circuit. It is observed that excitons closer to the electrode are slightly more dynamic. The steady–state is reached faster when the exciton formation rate increases. For SC condition, the time of steady–state is shorter than for OC and independent on the value of k_f (see figure S11 in Supplementary data). It originates from a higher level of electric field for J_{sc} and therefore the exciton formation rate does not influence neither dynamics of photocurrent nor excitons concentration.

Figure 6 shows a spatial distribution of excitons (for the case of OC) calculated for three times equal to 0 ps, 100 ps and 2 ns which represent a time counting after generation is turned on ($G \neq 0$). These times have been chosen in a way that there is no illumination (0 ps), the light–soaking has already taken place (100 ps) and the steady–state condition has been reached (2 ns). It is seen that at 0 ps the shapes of excitons distribution for high (part a), intermediate (part b) and low (part c) values of k_f are similar due to negligible influence of illumination. However, when the generation is turned on, we observe an increase of excitons for high and intermediate formation rates

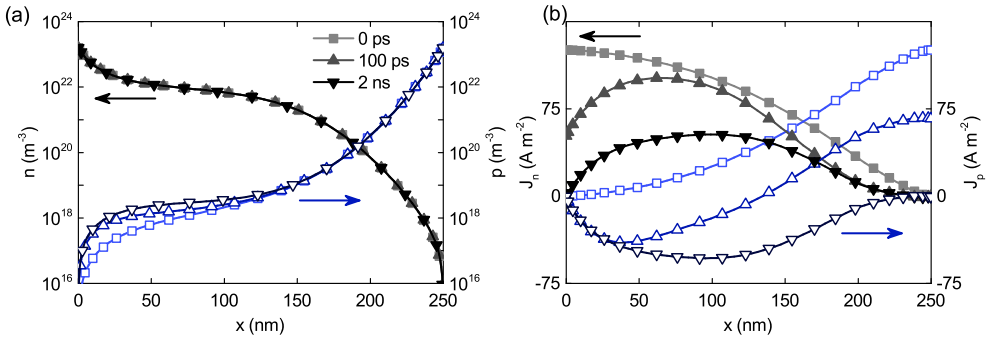

Figure 7. Simulation results for open–circuit (V_{oc}) at 295 K. Spatial distributions of a) electrons (closed symbol) and holes (open symbol) concentrations, and b) electron (closed symbol) and hole (open symbol) currents. Squares, upper triangles and lower triangles denote spatial distributions for 0 ps, 100 ps and 2 ns, respectively, which is a time since generation was turned on ($G \neq 0$). The exciton formation rate (k_f) is equal to 10^{-11} m^3 s^{-1}.

but only close to the anode. Figure 7(a) presents results for $k_f = 10^{-11}$ m^3 s^{-1} obtained for OC condition. Here, we can notice that light generates more holes near the anode. Therefore, excitons created with a high formation rate occur because light increases the concentration of holes which approach electrons that are major charge carriers in this region. The spatial distribution of photocurrent is also established for an open–circuit when an illumination is turned on [see figure 7(b)]. We can see that the influence of illumination on charge carriers is negligible for intermediate and low formation rates, as shown in figures S13–S14 in Supplementary data. For SC condition, where steady–state is reached faster, the analysis has been performed for times 1 ps, 10 ps and 1 ns after light has been switched on (see figure S12 in Supplementary data). As observed, the light generates electrons and holes in the bulk of the sample which causes an increasing of photocurrent and excitons. For the case without illumination, the charge carriers densities are very low within the sample as there is no external energy to excite them to a higher energy level. Therefore, the exciton concentration is about zero (results not presented here).

3.2. Results for 80 K

The next step is to analyze the impact of excitons at low temperature. As it was mentioned before, the perovskite material changes phase with temperature which influences its properties. The most importantly, the exciton binding energy is increasing for orthorhombic phase to about 34 meV (see Ref. 49) which is now higher than the thermal energy (6 meV at 80 K). This may suggest higher stability of the produced exciton in lower temperature. However, Wang et al.[20] have reported that the exciton lifetime is much shorter and decreases to about 3 ps. It is still not clear what is a type of excitons in organo-lead halide perovskite materials at low temperature. Although, one can find a hypothesis that such excitons are of Wannier type[21,50] but this assumption

Table 2. Parameters for simulation at 80 K.

Parameter	Symbol	Value	
Exciton binding energy	E_B	34 meV	Ref. 49
Dielectric constant	ε_r	39.39	Ref. 15
Mobility of electrons	μ_n	143 cm^2 V^{-1} s^{-1}	Ref. 14
Mobility of holes	μ_p	143 cm^2 V^{-1} s^{-1}	Ref. 14
Exciton decay time	τ_s	3 ps	Ref. 20
e^- and h^+ capture coefficients	C_n, C_p	3.18×10^{-15} m^3 s^{-1}	Ref. 14
e^- and h^+ Auger constants	Γ_n, Γ_p	23.4×10^{-40} m^6 s^{-1}	Ref. 14
Edge of conduction band	E_c	−3.9 eV	Ref. 19
Edge of valence band	E_ν	−5.5 eV	Ref. 19
Reduction factor	ξ	1.66×10^{-4}	Ref. 14

requires further studies to prove it. The difficulties arrise when finding experimental values of k_f at low temperatures as it has not been measured in perovskite materials yet. The bimolecular formation rate depends strongly on temperature and it increases by orders of magnitude when lowering the lattice temperature of semiconductor[34,51–53]. Therefore, we have decided to choose magnitudes of exciton formation rate which represent general tendency observed in semiconductors. For low temperature simulation k_f is equal to 10^{-7}, 10^{-9} and 10^{-11} m^3 s^{-1}, called in this paragraph high, intermediate and low exciton formation rates, respectively. In the absence of experimental data (κ and η parameters) for $CH_3NH_3PbI_3$ material at low temperature, the generation profile has been used the same as at room temperature, see figure 1(b). Other parameters, which are presented in table 2, have been adopted from literature for the perovskite material (80 K).

Figure 8(a) shows J–V characteristics calculated using the values of k_f from above. First, it should be noticed that V_{oc} is shifted about 0.35 V, if a temperature changes

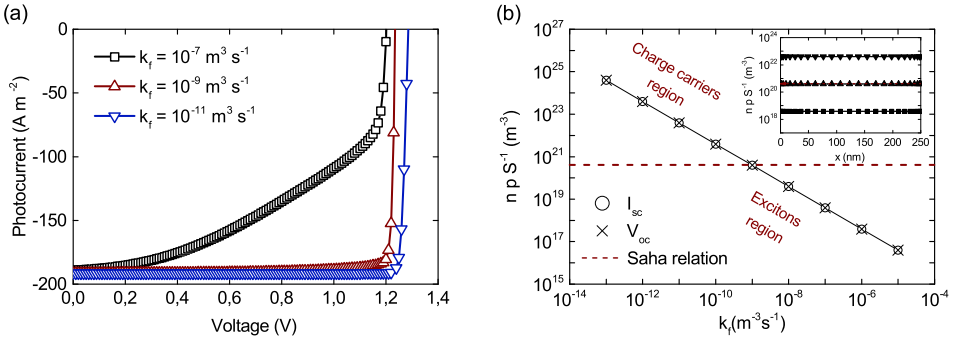

Figure 8. Simulation results for different exciton formation parameters at 80 K. a) J–V characteristics, b) a Saha relation for J_{sc} (circle symbol) and V_{oc} (cross symbol) with red line showing equilibrium level between charge carriers and excitons. An inset shows spatial distribution of Saha relation. Squares, upper triangles and lower triangles denote the exciton formation rates (k_f) equal to 10^{-7}, 10^{-9} and 10^{-11} m^3 s^{-1}, respectively.

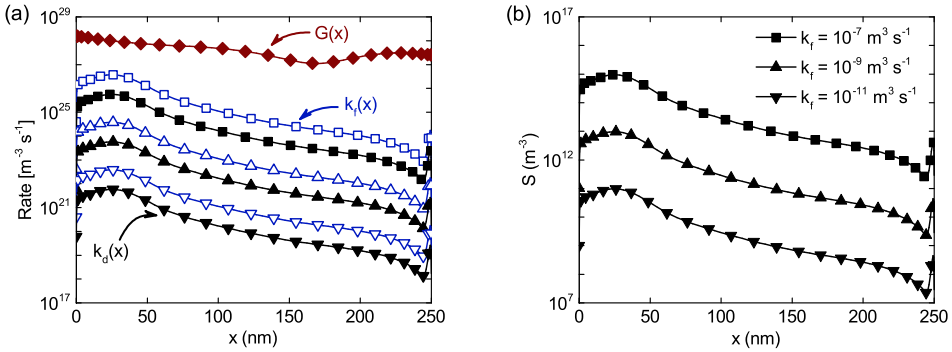

Figure 9. Simulation results for short–circuit current (J_{sc}) at 80 K. a) Exciton formation, dissociation and charge carrier generation rates, b) exciton density distribution. The diamond symbols indicate the rate of charge carriers generation. Squares, upper triangles and lower triangles denote the exciton formation rates (k_f) equal to 10^{-7}, 10^{-9} and 10^{-11} m^3 s^{-1}, respectively. The closed symbol is used for the formation rate and open symbol represents the dissociation rate of excitons.

from 295 K to 80 K for the same exciton formation rate equal to 10^{-11} m^3 s^{-1}. The same tendency has been observed by Shao et al.[54] for the OTP solar cell, where a decreasing temperature (from 295 K to 140 K) has increased V_{oc} by about 0.15 V. Second, the impact of exciton formation rate is the same as for tetragonal phase, where the rise of k_f causes that a value of V_{oc} increases but J_{sc} is the same. The Saha relation once again shows a flat distribution in space; see figure 8(b). For a low value of the exciton formation rate, electrons and holes dominate in the OTP solar cell. However, for the intermediate k_f, we observe an equilibrium between free charge carriers and excitons which means that there is no dominant part. Therefore, even a small increase of the formation rate would lead to dominance of excitons in the $CH_3NH_3PbI_3$ absorber layer, as observed for high k_f.

Figure 9(a) shows a comparison of the generation, dissociation and exciton formation rates calculated for SC condition. It is clearly seen that the probability of a generation process is around two orders of magnitude higher than for formation and dissociation mechanisms. Therefore, we can conclude that excitons prevail in the OTP solar cell at the orthorhombic phase (at low temperature). It is also possible that the formation rate could be even higher for lower temperatures, however to formulate final conclusion there is a need for experimental confirmation which is not an aim of this paper. In figure 9(a), we can also observe that the rates of the exciton formation and the dissociation, presented as a function of a distance from the electrode, both follow the distribution of excitons [see figure 9(b)]. However, the rates are not equal and the formation process is more possible than a dissociation due to a monomolecular recombination of excitons. Therefore, for a high value of τ_S, a probability of this recombination is rather low. It means that almost all free electrons and holes are produced back from excitons (see figure S23 in Supplementary data). Although, for smaller τ_S, the recombination competes with other processes and, as a consequence,

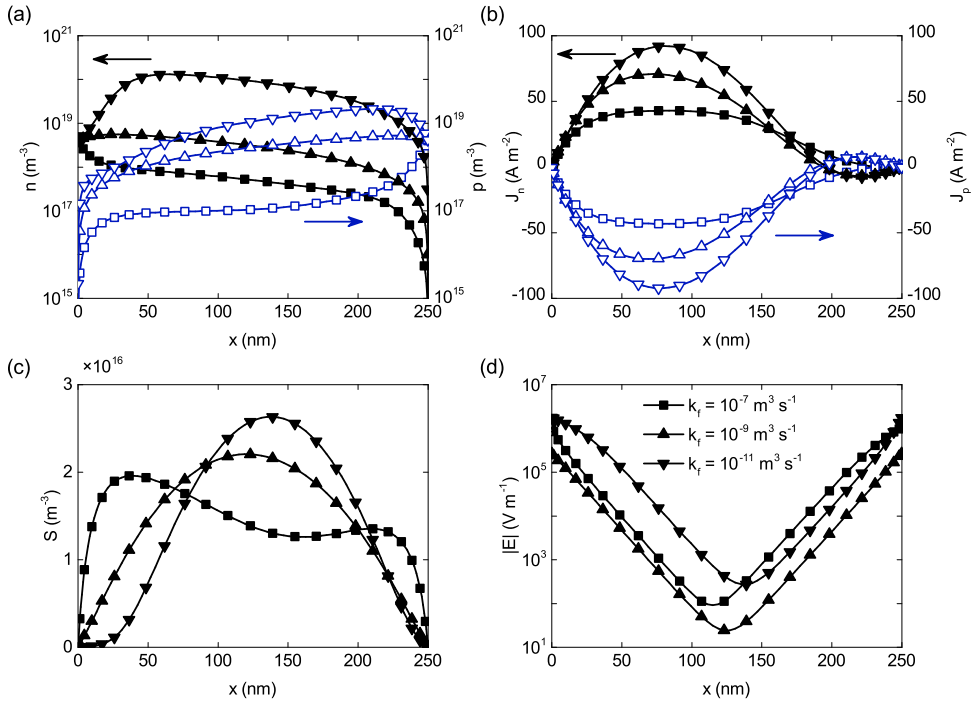

Figure 10. Simulation results for open–circuit (V_{oc}) at 80 K. Spatial distribution for a) electrons (closed symbol) and holes (open symbol) concentrations, b) electron (closed symbol) and hole (open symbol) photocurrents, c) exciton concentration, and d) electric field. Squares, upper triangles and lower triangles denote the exciton formation rates (k_f) equal to 10^{-7}, 10^{-9} and 10^{-11} m^3 s^{-1}, respectively.

not all excitons dissociate. This conclusion supports the statement that excitons are dominant in the OTP solar cell at low temperature and the excitonic mechanisms should influences the operation of the low temperature devices.

Once again, the nonuniform generation and the presence of mobile ions cause irregular shapes of charge carriers densities and photocurrents in space. Therefore, in order to eliminate non–physical analysis, we also simulated the OTP photocell at low temperature with uniform generation and with immobile ions. It is seen that nonuniform generation is mostly affecting the distributions of photocurrents J_n and J_p, as shown in figures S16–S17 in Supplementary data. However, the existence of mobile ions drastically changes the distribution of electric field which impacts the electron, hole and exciton concentrations, especially for SC condition where almost all ions accumulate at one electrode; see figure S20 (Supplementary data). In the case of OC, the impact of ions calculated for the intermediate k_f is only observed in the visible change of the electric field distribution, where the highest value is visible at the electrodes and almost zero in the middle of the sample, as depicted in figure S21 (Supplementary data). However, for a high value of the formation rate, the total concentration of charge carriers is decreased and shifted toward the cathode [figure S2(a) in Supplementary data]. It causes that electrons and holes create more excitons in the same position resulting in the observed

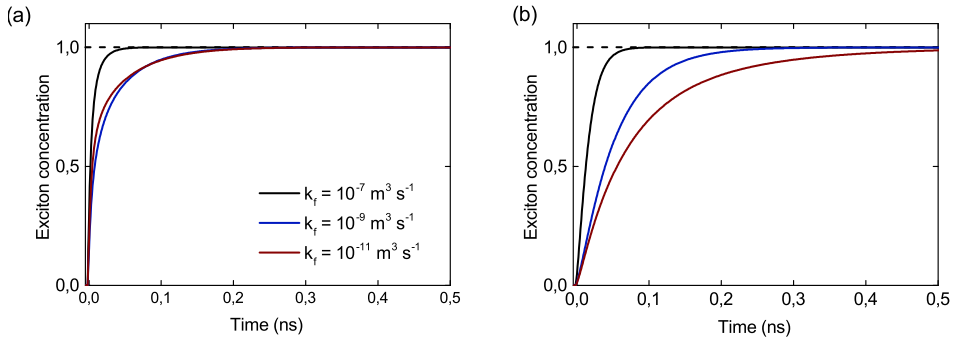

Figure 11. Simulation results for open-circuit (V_{oc}) at 80 K. Transient results for exciton concentration a) at the position close to the anode, and b) in the middle of sample. Black, blue and red lines denote the exciton formation rates (k_f) equal to 10^{-7}, 10^{-9} and 10^{-11} m^3 s^{-1}, respectively. All results are normalized.

peak at about 220 nm; see figure S22(b) in Supplementary data.

Figure 10 illustrates spatial results presented for different exciton formation rates calculated for OC. We can see that the electron and hole concentrations are the highest in the middle of the sample for a low formation rate. Equations (14–18) clearly show that the density of carriers near electrodes should decrease for lower temperatures. For higher values of k_f, the total concentrations of n and p are lower in the bulk of the sample relatively to the position which is closer to the metal electrode. As shown in figure 10(b), the formation rate also affects the spatial distribution of photocurrents J_n and J_p. It can be noticed that the both photocurrents decrease for higher k_f. This is directly influenced by a change of charge carrier concentration and also by an electric field distribution ($|E|$). An absolute value originates from the relation $V_{oc} > V_{built}$ which leads to negative values of electric field [figure 10(d)]. As illustrated in figure 10(c), the shape of excitons distribution spreads more uniformly across the sample and a total density of excitons slightly increases only for higher formation rate. The observed shape of S is most likely due to the drastic decrease of charge carrier concentration in the middle of OTP solar cell. Under the SC condition, there is negligible change of space charge carriers and related currents J_n and J_p for different k_f; see figure S24 in Supplementary data.

Figure 11 illustrates transient results of the exciton concentration obtained for two spatial points, meaning close to the anode and in the middle of the $CH_3NH_3PbI_3$ absorber layer (both for V_{oc}). It can be noticed that the observed dynamics at low temperature is about order of magnitude faster than for room temperature. This effect originates because the processes of exciton formation and monomolecular recombination need shorter times for the orthorhombic phase; see table 2. We also observe that the steady–state condition is reached much faster for the position closer to the electrode than in the middle of the sample. In figure 11(a), it is visibly seen that the higher formation rate drastically increases dynamics. However, for intermediate and low values, we obtained approximately the same results. In the bulk of the $CH_3NH_3PbI_3$ layer, the

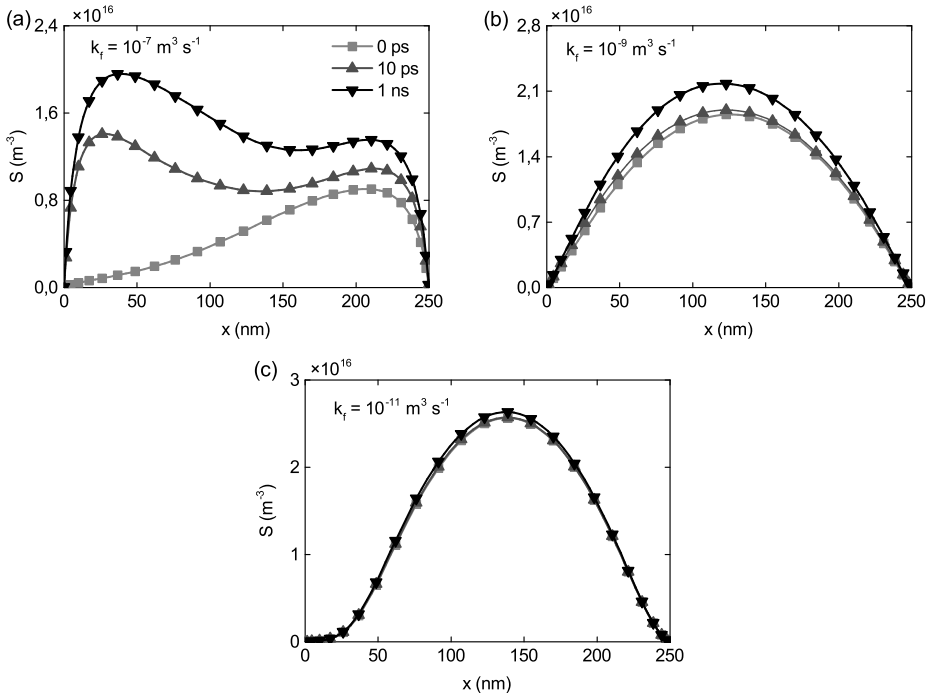

Figure 12. Simulation results for open–circuit (V_{oc}) at 80 K. Spatial distributions for exciton formation rate (k_f) equal to a) 10^{-7}, b) 10^{-9}, and c) 10^{-11} m^3 s^{-1}. Squares, upper triangles and lower triangles denote spatial distributions for 0 ps, 10 ps and 1 ns, respectively, which is a time since generation was turned on ($G \neq 0$).

dynamics is getting higher with the exciton formation rate [figure 11(b)]. Therefore, in contrast to simulations at room temperature, a rise of the concentration S depends not only on the rate k_f but also on the position in the device. At the SC state, the observed dynamics is really high and independent of the exciton formation rate and the position; see figure S25 in Supplementary data.

Figure 12 shows spatial distributions of excitons calculated for three times equal to 0 ps, 10 ps and 1 ns after illumination (OC condition). It is observed that without illumination (0 ps), the maximum density of excitons is shifted toward the cathode for higher exciton formation rate, and to the middle of the sample for the lower rate. When the generation (G) is turned on, there is a visible increase in exciton density observed only for high and intermediate values of k_f. Figure 12(a) illustrates that a concentration S drastically increases close to the anode for the high k_f. Similarly to results reported for a room temperature, this effect is due to a higher hole density which influences the creation of electron–hole pairs after illumination [figure 13(a)]. In figure 13(b), we can see the photocurrent distributions of J_n and J_p obtained for V_{oc}. For the case when the generation is turned on, both currents are distributed symmetrically about the zero value. For the low and intermediate exciton formation rates, an impact of illumination is smaller; see figures S27–S28 in Supplementary data. Additionally, as observed in figure S26(a) which illustrates the case of SC condition calculated with intermediate exciton formation rate, the hole density also increases throughout the OTP

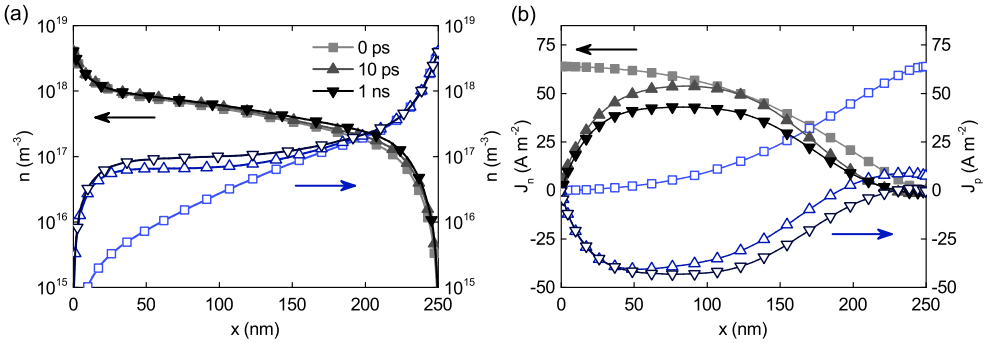

Figure 13. Simulation results for open–circuit (V_{oc}) at 80 K. Spatial distributions of a) electrons (closed symbol) and holes (open symbol) concentrations, and b) electron (closed symbol) and hole (open symbol) currents. Squares, upper triangles and lower triangles denote spatial distributions for 0 ps, 10 ps and 1 ns, respectively, which is a time since generation was turned on ($G \neq 0$). The exciton formation rate (k_f) is equal to 10^{-7} m^3 s^{-1}.

solar cell just after illumination. Obviously, the change of charge carriers concentration influences the photocurrent distribution within the sample; see figure S26(b). When the generation is turned on, the average value of exciton density increases in the bulk of the $CH_3NH_3PbI_3$ absorber layer, imitating the shape of a hole density. It suggests that holes, which are less mobile in the OTP solar cells, take a crucial part in the process of the excitons creation.

4. Summary

In summary, we have analyzed an impact of excitons in the organometal trihalide perovskite $CH_3NH_3PbI_3$ solar cell for tetragonal and orthorhombic phases. The calculations have been carried out based on the validated space and time drift–diffusion model. A very good agreement has been found between theoretical and experimental J–V characteristics for several thicknesses of the device. We have shown that excitons cannot dominate in the material at room temperature but they might be in an equilibrium with free electrons and holes. However, the excitons can prevail in the perovskite material at an orthorhombic phase. We have also confirmed that the impact of excitons formation is mostly observable for a case of an open circuit. The excitonic effects are clearly visible by lowering charge carrier concentrations in the middle of sample which causes decreasing of V_{oc}. This work provides new facts about photophysical processes in the lead halide perovskite, which might be useful for the photovoltaics especially for low temperature operation in space environment for powering satellites.

5. Supplementary data

See Supplementary data at ... for more detailed description of numerical methods, parameters used in the transfer–matrix model for calculating generation profiles and

additional modeling results for 295 K and 80 K temperatures.

6. Acknowledgment

Calculations were carried out at the Academic Computer Centre (CI TASK) in Gdańsk.

References

[1] Zhao D, Wang C, Song Z, Yu Y, Chen C, Zhao X, Zhu K and Yan Y 2018 *ACS Energy Lett.* **3** 305–306
[2] Zhu X, Yang D, Yang R, Yang B, Yang Z, Ren X, Zhang J, Niu J, Feng J and Liu S F 2017 *Nanoscale* **9** 12316–12323
[3] Yang W S, Park B W, Jung E H and Jeon N J 2017 *Science* **356** 1376–1379
[4] Wehrenfennig C, Eperon G E, Johnston M B, Snaith H J and Herz L M 2014 *Adv. Mater.* **26** 1584–1589
[5] Stranks S D, Eperon G E, Grancini G, Menelaou C, Alcocer M J P, Leijtens T, Herz L M, Petrozza A and Snaith H J 2014 *Science* **342** 341–344
[6] Park N G 2015 *Mater. Today* **18** 65–72
[7] Green M A, Jiang Y, Soufiani A M and Ho-Baillie A 2015 *J. Phys. Chem. Lett* **6** 4774–4785
[8] Yamada Y, Nakamura T, Endo M, Wakamiya A and Kanemitsu Y 2015 *IEEE J. Photovolt.* **5** 401–405
[9] Lin Q, Armin A, Nagiri R C R, Burn P L and Meredith P 2015 *Nat. Photonics* **9** 106–112
[10] Miyata A, Mitioglu A, Plochocka P, Portugall O, Wang J T W, Stranks S D, Snaith H J and Nicholas R J 2015 *Nat. Phys.* **11** 582–587
[11] D'Innocenzo V, Grancini G, Alcocer M J P, Kandada A R S, Stranks S D, Lee M M, Lanzani G, Snaith H J and Petrozza A 2014 *Nat. Commun.* **5** 3586
[12] Saba M, Quochi F, Mura A and Bongiovanni G 2016 *Acc. Chem. Res.* **49** 166–173
[13] Głowienka D, Miruszewski T and Szmytkowski J 2018 *Solid State Sci.* **82** 19 – 23
[14] Milot R L, Eperon G E, Snaith H J, Johnston M B and Herz L M 2015 *Adv. Funct. Mater.* **25** 6218–6227
[15] Onoda-Yamamuro N, Matsuo T and Suga H 1992 *J. Phys. Chem. Solids* **53** 935–939
[16] Maynard B, Long Q, Schiff E A, Yang M, Zhu K, Kottokkaran R, Abbas H and Dalal V L 2016 *Appl. Phys. Lett.* **108** 1–5
[17] Stoumpos C C, Malliakas C D and Kanatzidis M G 2013 *Inorg. Chem.* **52** 9019–9038
[18] Kawamura Y, Mashiyama H and Hasebe K 2002 *J. Phys. Soc. Jpn.* **71** 1694–1697
[19] Baikie T, Fang Y, Kadro J M, Schreyer M, Wei F, Mhaisalkar S G, Grätzel M and White T J 2013 *J. Mater. Chem. A* **1** 5628–5641
[20] Wang H, Whittaker-Brooks L and Fleming G R 2015 *J. Phys. Chem. C* **119** 19590–19595

[21] Hirasawa M, Ishihara T, Goto T, Uchida K and Miura N 1994 *Physica B* **201** 427–430
[22] Miyazawa Y, Ikegami M, Chen H W, Ohshima T, Imaizumi M, Hirose K and Miyasaka T 2018 *Science* **2** 148 – 155
[23] Wang Z S, Sha W E I and Choy W C H 2016 *J. Appl. Phys.* **120** 213101
[24] Hwang I and Greenham N C 2008 *Nanotechnology* **19** 424012
[25] Barker J A, Ramsdale C M and Greenham N C 2003 *Phys. Rev. B* **67** 075205
[26] Głowienka D and Szmytkowski J 2017 *Acta Phys. Pol. A* **132** 397–400
[27] Calado P, Telford A M, Bryant D, Li X, Nelson J, O'Regan B C and Barnes P R F 2016 *Nat. Commun.* **7** 13831
[28] Van Reenen S, Kemerink M and Snaith H J 2015 *J. Phys. Chem. Lett* **6** 3808–3814
[29] Ren X, Wang Z, Sha W E I and Choy W C H 2017 *ACS Photonics* **4** 934–942
[30] Richardson G, O'Kane S, Niemann R G, Peltola T, Foster J M, Cameron P J and Walker A 2016 *Energy Environ. Sci.* **9** 1476–1485
[31] Sherkar T S, Momblona C, Gil-Escrig L, Bolink H J and Koster L J A 2017 *Adv. Energy Mater.* **7** 1602432
[32] Zhou Y and Gray-Weale A 2015 *Phys. Chem. Chem. Phys.* **18** 4476–4486
[33] Walter D, Fell A, Wu Y, Duong T, Barugkin C, Wu N, White T and Weber K 2018 *J. Phys. Chem. C* **122** 11270–11281
[34] Piermarocchi C, Tassone F, Savona V, Quattropani A and Schwendimann P 1997 *Phys. Rev. B* **55** 1333–1336
[35] Stranks S D, Burlakov V M, Leijtens T, Ball J M, Goriely A and Snaith H J 2014 *Phys. Rev. Applied* **2**(3) 034007
[36] Selberherr S 1984 *Analysis and Simulation of Semiconductor Devices* (Springer-Verlag Wien)
[37] Simmons J G and Taylor G W 1971 *Phys. Rev. B* **4** 502–511
[38] Langevin P 1903 *Ann. Chim. Phys.* **28** 433
[39] Beattie A R and Landsberg P T 1959 *Proc. Royal Soc. A* **249** 16–29
[40] Scharfetter D L and Gummel H K 1969 *IEEE Trans. Electron Devices* **16** 64–77
[41] Roghabadi F A, Aghmiuni K O and Ahmadi V 2016 *Org. Electron.* **34** 164 – 171
[42] Xiao Z, Dong Q, Bi C, Shao Y, Yuan Y and Huang J 2014 *Adv. Mater.* **26** 6503–6509
[43] Kim H S, Lee C R, Im J H, Lee K B, Moehl T, Marchioro A, Moon S J, Humphry-Baker R, Yum J H, Moser J E, Grätzel M and Park N G 2012 *Sci. Rep.* **2** 591
[44] Pettersson L A A, Roman L S and Inganäs O 1999 *J. Appl. Phys.* **86** 487–496
[45] Burkhard G F, Hoke E T and McGehee M D 2010 *Adv. Mater.* **22** 3293–3297
[46] Saha M N 1921 *Proc. Royal Soc. A* **99** 135
[47] Valverde-Chávez D A, Ponseca C, Stoumpos C, Yartsev A, Kanatzidis M G, Sundström V and Cooke D G 2015 *Energy Environ. Sci.* **8** 3700–3707
[48] Głowienka D and Szmytkowski J 2018 *Chem. Phys.* **503** 31–38
[49] Sestu N, Cadelano M, Sarritzu V, Chen F, Marongiu D, Piras R, Mainas M, Quochi F, Saba M, Mura A and Bongiovanni G 2015 *J. Phys. Chem. Lett.* **6** 4566–4572

[50] Zhang H, Qiao X, Shen Y, Moehl T, Zakeeruddin S M, Grätzel M and Wang M 2015 *J. Mater. Chem. A* **3**(22) 11762–11767
[51] Selbmann P E, Gulia M, Rossi F, Molinari E and Lugli P 1996 *Phys. Rev. B* **54**(7) 4660–4673
[52] Kira M, Hoyer W, Stroucken T and Koch S W 2001 *Phys. Rev. Lett.* **87**(17) 176401
[53] Janković V and Vukmirović N 2015 *Phys. Rev. B* **92**(23) 235208
[54] Shao S, Liu J, Fang H H, Qiu L, ten Brink G H, Hummelen J C, Koster L J A and Loi M A 2017 *Adv. Energy Mater.* **7** 1701305